

13th CIRP Conference on Photonic Technologies [LANE 2024], 15-19 September 2024, Fürth, Germany

Ultra-short pulse laser ablation of metals: A comprehensive 3D simulation perspective enlightening novel process insights

Tobias Florian^{a,*}, Michele Buttazzoni^a, Constantin Zenz^a, Andreas Otto^a

^aTU Wien, Institute of Production Engineering and Photonic Technologies, Getreidemarkt 9/BA09, 1060 Wien, Austria

* Corresponding author. Tel.: +43-1-58801-311628. E-mail address: tobias.florian@tuwien.ac.at

Abstract

Intricate dynamics in ultra-short pulse laser ablation of metals necessitate deeper process understanding. This work presents an auspicious contribution in this direction, incorporating a sophisticated three-dimensional finite-volume simulation tool, building upon our previously validated models in continuous-wave laser material processing. Atop the existing multiphysics framework, a two-temperature and a Drude absorption model has been integrated. Focused on laser ablation of copper, preliminary results unveil novel perspectives on the dynamic interaction between thermal effects and material response. Surpassing limitations inherent in one- and two-dimensional descriptions, this model distinctively captures the complex interplay of electron heating, energy transfer to the lattice, and ensuing rapid phase transitions. Crucially, it complements existing insights into ablation mechanism by illustrating the influence of elusive temperature-dependent material properties, such as density and the bulk modulus for superheated liquid metal, on the process. While still in development, these advancements mark a promising stride towards a deeper process comprehension.

© 2024 The Authors. Published by Elsevier B.V.

This is an open access article under the CC BY-NC-ND license (<https://creativecommons.org/licenses/by-nc-nd/4.0>)

Peer-review under responsibility of the international review committee of the 13th CIRP Conference on Photonic Technologies [LANE 2024]

Keywords: Laser material micro processing; Pulsed laser material ablation of metals; Multiphysics process simulation; Two-temperature model

1. Introduction

Ultra-short pulse laser ablation of metals is at the forefront of advanced materials processing, offering precision engineering with minimal thermal damage. Due to the intricate dynamics and the challenges of in-situ process monitoring, a comprehensive process understanding remains elusive. Recently, an increasing number of research groups have committed to filling this gap in knowledge via numerical simulations and analyses. Current methodologies to investigate short and ultra-short pulse laser ablation such as TTM (two-temperature models), MD (molecular dynamic) models, hybrid TTM-MD models and HD (hydrodynamic models) have been studied and summarized in [1]. These existing models collectively form a substantial foundation of knowledge, each with its own set of strengths and restrictions. While e.g., MD or

TTM-MD models aim to elucidate the ablation mechanism at atomistic scales, our 3-dimensional simulation framework endeavors to describe the entire process: Laser beam propagation and absorption, electron heating, electron-phonon coupling, material response and phase changes, evolution of shock waves and tracking of ablated material. This thorough approach is designed to capture the complex, mostly non-linear interplay of events at a mesoscopic point of view with the objective of predicting and explaining holistic crater topology and drill hole features.

In order to incorporate the non-equilibrium physics between the electron and lattice temperature, the finite volume based multiphysics model, recently published in [2], has been extended by a Drude absorption model and the two-temperature model, described below (Section 2.1).

Further, the model is used to simulate single pulse (120fs) ablation of copper with an 800nm wavelength laser over a fluence spectrum of 6.1 to 63.4J/cm². These processing parameters have recently been investigated numerically and experimentally by [3]. The results achieved by the simulations are in good agreement with the experiments and offer valuable insights in the ablation mechanisms and crater formation.

2. Methods and Materials

2.1. Simulation Model

Building upon the simulation approach comprehensively outlined and discussed in our previous publication [2], this work supplements the equilibrium model to cope with the complexities inherent in ultra-short pulse laser processes by including a two-temperature model and a Drude absorption model. For the sake of brevity, the essential features of the base model will be concisely elaborated and only the complementing formulas will be given in the following. For a detailed investigation of the OpenFOAM based simulation model, we refer the reader to study [2].

The Mass-of-Fluid model ensures the conservation of mass, energy and momentum by tracking mass and energy across multiple materials in their respective aggregation states (e.g. having one metallic process material, we encounter the phases *solid metal*, *liquid metal*, *metal vapor* and the *ambient gas*). In order to capture trans and supersonic phenomena such as shock waves typically occurring in laser micro processing, the approach models the fluid flow via the compressible Navier Stokes equations in a mixture formulation. Phase changes including melting, solidification, evaporation, condensation and sublimation are directly integrated through the exchange of mass and energy between phase-pairs. Thereby, evaporation-induced recoil pressure is inherently an implicit result, eliminating the need for an explicit formulation. Pressure-driven evaporation and condensation are modeled on the principles of Hertz-Knudsen with the saturation pressure determined by the Clausius-Clapeyron equation. Furthermore, the reduction of latent heat of vaporization towards the critical temperature T_{crit} is incorporated via the Watson correction, making an explicit phase explosion model obsolete. As mass and energy is transferred through evaporation, our model directly couples evaporation and pressure changes, since the creation of vapor locally increases volume and pressure, and thus limits further evaporation. Thereby, this method omits the need for evaporation and condensation efficiencies leveraging the predictive power of the model.[2]

When it comes to ultra-short laser pulses, the electron temperature T_e rises faster than the heat can be transferred to the lattice and diffuse away from the illuminated area [4]. Since the absorption of laser light is non-linearly dependent on the electron temperature, a two-temperature model as well as a sophisticated absorption model must be included. As described in [5], the electron and lattice temperature T_e and T_l follow the formulas

$$\frac{\partial(C_e T_e)}{\partial t} = \nabla \cdot (\lambda \nabla T_e) - C_e \nabla(\mathbf{u} T_e) - G(T_e - T_l) + Q_{abs} \quad (1)$$

and

$$\frac{\partial(C_l T_l)}{\partial t} = -C_l \nabla(\mathbf{u} T_l) + G(T_e - T_l), \quad (2)$$

where $C_e(T_e)$ and $C_l(T_l)$ are the heat capacities of the electrons and lattice, $G(T_e)$ is the electron phonon coupling factor, $\lambda(T_e)$ is the electron thermal conductivity, \mathbf{u} the velocity of the multiphase mixture and $Q_{abs}(T_e, Intensity)$ is the absorbed laser energy. Since heat conduction and laser absorption are predominantly driven by the electrons, the lattice thermal conductivity and the laser absorption source term in the lattice energy equation in [2] have to be set zero. Consistently to the treatment of the lattice energy equation in [2], also the electron energy equation is decoupled into convective and conductive transport.

The procedure to calculate the last missing ingredient Q_{abs} in Eqn. (1) resembles the one examined in [2]: In this study, we only examine Gaussian laser beams with normal incident angle to the metal surface. Moreover, only single femtosecond laser pulses are involved, hence plasma and vapor absorption can be neglected [5]. This cancels out various terms in the Radiative Transport Equation (cf. Eqn. 39 and 40 in [2]). In fact, for calculating the reflectivity R in Eqn. 43 in [2] and the absorptivity of condensed matter ζ_{cond} we only need the complex refractive index $\bar{n} = n + i\kappa$ and the nonlinear term ζ_{NL} . The latter incorporates non-equilibrium electrons that penetrate the non-excited region at Fermi velocity. As in [3], this term is calculated as

$$\zeta_{cond} = \sqrt{\frac{2k_B T_e}{m_e}} \cdot t_b, \quad (3)$$

with k_B , m_e and $t_b = 27$ fs [12] being the Boltzmann constant, the electron mass and the Drude relaxation time. The refractive index n and extinction coefficient κ are obtained as

$$\bar{n} = n + i\kappa \begin{cases} n = \sqrt{\frac{|\bar{\epsilon}| + \epsilon_R}{2}} \\ \kappa = \sqrt{\frac{|\bar{\epsilon}| - \epsilon_R}{2}} \end{cases} \quad (4)$$

with the complex dielectric permittivity $\bar{\epsilon}$

$$\bar{\epsilon} = \epsilon_R + i\epsilon_I \begin{cases} \epsilon_R = 1 - \frac{\omega_p^2}{\omega^2 + v_{eff}^2} \\ \epsilon_I = \frac{\omega_p^2 v_{eff}}{\omega(\omega^2 + v_{eff}^2)} \end{cases} \quad (5)$$

with ω_p , the electron plasma frequency, ω , the laser light frequency and v_{eff} , the effective collision frequency following the calculations in [6]. The remaining calculation procedure follows the one outlined in [2].

2.2. Simulation Setup

The simulation setup is designed to imitate the experiments carried out in [3]: A single Gaussian laser pulse of 120fs duration (at FWHM) and wavelength of 800nm with spatial Gaussian distribution with an effective focused beam diameter of 6.5 μ m irradiates a pure copper foil. The ambient gas is air, initially at atmospheric pressure. Simulations are conducted for four different pulse energies, namely 1.0, 3.8, 7.4 and 10.4 μ J

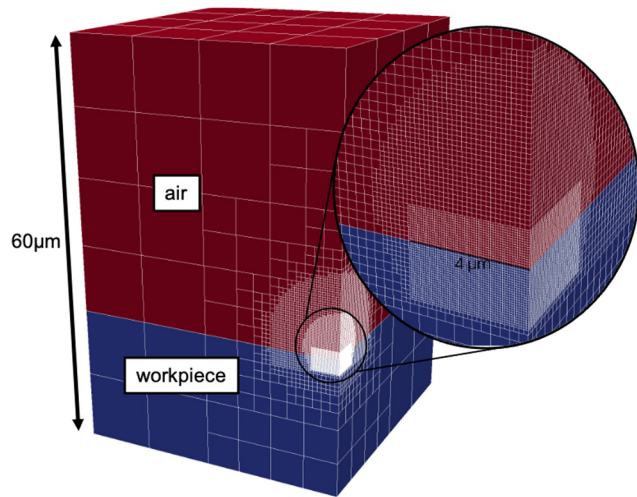


Fig. 1. Finite volume mesh with initial material distribution.

with respective fluences of 6.1, 23.2, 45 and 63.4J/cm², which is significantly higher than the ablation threshold of 0.5J/cm², simulated by [3]. In order to save computation costs, the finite volume domain is simulated as a quarter domain, as can be seen in Fig.1 – symmetric boundary conditions are employed respectively. The domain expands over a copper foil of 20μm depth and, expanding the symmetry, 80μm×80μm width. On top, the atmosphere is modeled 40μm above the surface. For the simulations with the three higher pulse energies, the largest and the smallest cells are 10μm and 78.125nm, and for the simulation with 1μJ, 5μm and 39.0625nm, yielding 7 refinement levels according to Fig 1.

The material properties of copper and its aggregate states as well as of ambient air are listed in Table 1. If not stated differently, the data resembles the one given in [2] for Cu-ETP.

Table 1. Material properties.

Property	T(K)	Value
Copper (general)		
Molar mass M (kg mol ⁻¹)	-	63.546 · 10 ⁻³
Solidus/Liquidus temperature (K)	-	1358
Boiling temperature (K)	-	2854
Critical temperature T_{crit} (K)	-	7696 [7]
Latent heat of fusion (m ² s ⁻²)	-	2.056 · 10 ⁵
Latent heat of vaporization (m ² s ⁻²)	-	4.75 · 10 ⁶
Copper (solid)		
Density (kg m ⁻³)	1358	8.35 · 10 ³ [8]
Bulk modulus (kg s ⁻² m ⁻¹)	1358	1.34 · 10 ¹¹
Electron thermal conductivity (kg m s ⁻³ K ⁻¹)	function of T_e and T_i	Eq. 12 in [3]
Electron heat capacity (kg m ⁻¹ s ⁻² K ⁻¹)	function of T_e	Fig. 1a in [3]
Electron phonon coupling factor (kg m ⁻¹ s ⁻³ K ⁻¹)	function of T_e	Fig. 1b in [3]
Copper (liquid)		
Density (kg m ⁻³)	1358	7.992 · 10 ³ [8]
	2854	6.792 · 10 ³ [8]
	7696	3.0 · 10 ³ [8]
Bulk modulus (kg s ⁻² m ⁻¹)	1358	7 · 10 ¹⁰ [9]

	2400	4 · 10 ¹⁰ [9]
	2855	5 · 10 ⁹
	6926	1 · 10 ⁷
	7696	1 · 10 ⁶
Tait exponent	-	1.0 [9]
Copper (vapor)		Same as in [2]
Air		Same as in [2]

Further details on the simulation setup such as boundary conditions can be disclosed upon request.

3. Results and discussion

In the following, we will first compare the simulated ablation depth versus the experimentally measured ones. Subsequently, the crater geometry will be analyzed and finally, the appearing ablation mechanisms will be discussed.

3.1. Ablation depth

Fig. 2 shows a good agreement between the simulated ablation depths with the experimentally measured ones over a broad spectrum of fluences. A minor trend can be seen that our model slightly overestimates the ablation depth for the two lower fluences at 6.1J/cm² 23.2J/cm² and conspicuously underestimates it at very high fluences at 63.4J/cm². The strong offset at this high fluence can have various reasons, starting with the relatively coarse mesh resolution that is used compared to 1- or 2-dimensional simulations. Given that the laser energy is absorbed within the first few cells, there might be an offset in the electron temperature and subsequent calculation of the refractive indices. Also, the ballistic electron penetration depth may be underestimated with the model in use for extremely high fluences, yielding too narrow energy deposition. Furthermore, the choice of temperature dependent material parameters such as the bulk modulus and density of the liquid metal at high temperatures could cause variations in the ablation depth, as will be discussed below (Section 3.3).

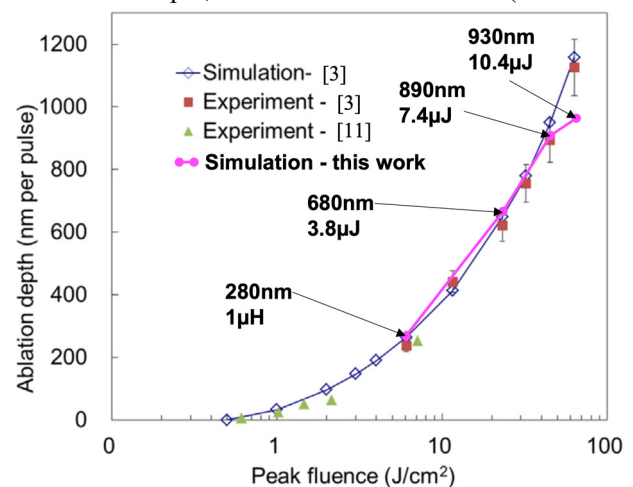


Fig. 2. Ablation depth vs. fluence comparison to experiment and simulation of [3,11]

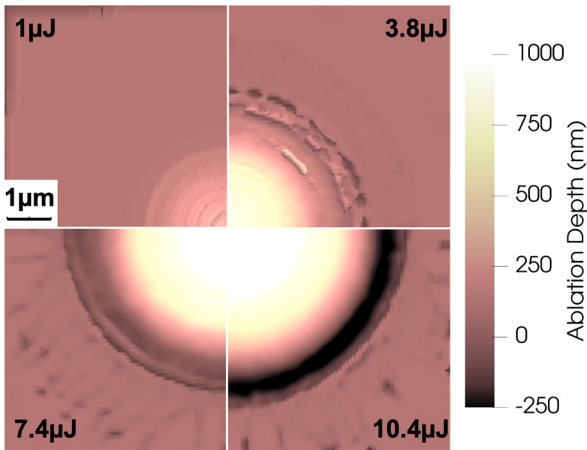


Fig. 3. Crater topologies carried out by simulations with 1, 3.8, 7.4 and 10.4 μJ pulse energies

3.2. Crater geometry

One of the strengths of our 3-dimensional model is its ability to predict crater topologies. The pulse impact geometries in Fig. 2 of [3] serve as the base to compare with our simulation results. For that, the top views of all four simulations are put together in Fig. 3, where also the ablation level throughout the crater is shown. Here, the general shapes and diameters match very well with the experiment. Notably, the occurrence of the ring-shaped structures is predicted accurately. The missing ring with the low energy pulse (1 μJ) suggests that no melt is ejected radially via the sides, whereas with increasing pulse energy (3.8 μJ), some spatters appear at the edge of the crater and the middle region exhibits a smoother and shiny surface. These characteristics are further reinforced with pulse energies 7.4 and 10.4 μJ.

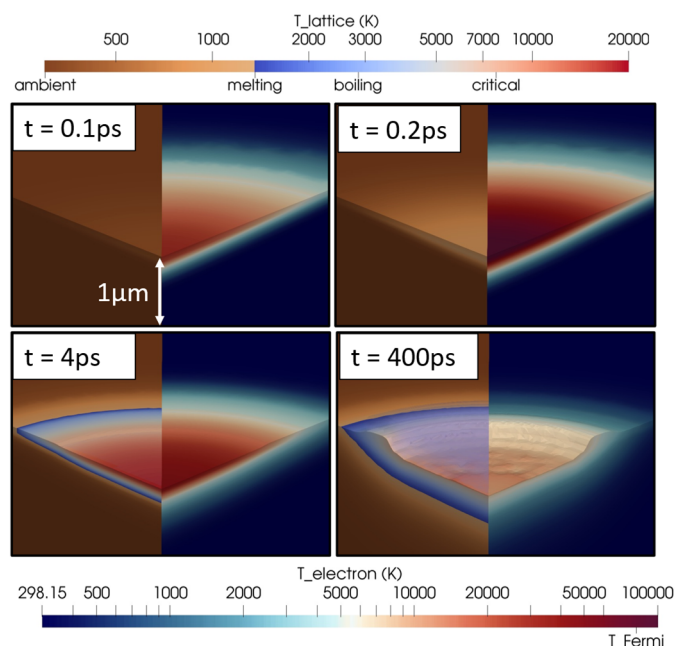


Fig.4. Electron vs. lattice temperature for 3.8 μJ pulse energy within first 400ps

3.3. Process mechanisms

In the following we will examine the process mechanisms that lead to the results discussed above. First of all, the snapshot sequence in Fig. 4 illustrates the evolution of the electron and lattice temperature in the 3.8 μJ simulation upon the first 400ps. Therein, only the region of interest, where the laser interacts with the material, is shown. On the left side of each frame, the lattice temperature, and on the right side, the electron temperature is shown at the workpiece – both in logarithmic scale. The electron temperature rises swiftly within laser illumination and reaches a maximum of 110000K. The sequence reveals the electron-phonon coupling upon the rise of the lattice temperature in copper, the generation of the melt pool and the onset of a vapor plume (visualized in transparent purple at t=400ps) depressing the melt pool.

Following the sequence in Fig. 3, which primarily involves mechanisms within the bulk, forthcoming investigations necessitate a slight modification to the visualization scheme. Fig. 5 illustrates the further development of the 3.8 μJ pulse process. Herein, the left side of the snapshot does not change – hence, the lattice temperature is shown at interpolated point values where the sum of liquid and solid material is more than 0.5, and again, the vapor in transparent purple. But now, on the right side, the density field is displayed to demonstrate shock waves, density changes within the condensed phases and density accumulations detaching the liquid metal. The first frame in Fig. 5 (at t=2.17ns) reveals that the evaporation has progressed (compared to the last frame in Fig. 4) and the high recoil pressure above the liquid surface (indicated by the significant vapor pressure level) further depresses the liquid metal to the sides. Moreover, a shock wave is traveling ahead of the expanding vapor plume. In this stage, the liquid temperature lies in the vicinity of the critical temperature. At the sides, the expansion of the liquid material overcomes the depressing vapor pressure, and a layer starts to detach. In the

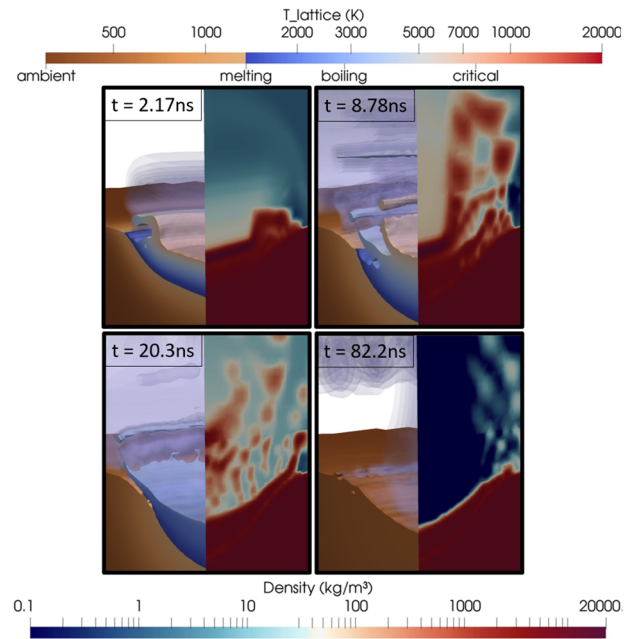


Fig.5. Ablation mechanism at 3.8 μJ pulse energy (680nm max. ablation depth)

next frame (at $t=8.78\text{ns}$), further layers of superheated fluid expel and quickly vaporize as soon as surrounding pressure falls below the equilibrium pressure. Next, at $t=20.3\text{ns}$, some dense liquid-vapor structures keep escaping from the surface, which can be seen only on the right side. In addition, a thin liquid layer is ejecting radially, which will consequence the ring structures at the final crater, which can be seen in the last frame, about 60ns later. Interestingly, the current vapor plume reminds of a mushroom cloud. All in all, this process shows a sequence of distinct ablation mechanisms: The phase transition from solid to liquid entails a fast volume change and thus a momentum away from the surface. Meanwhile, the strong evaporation at the surface pushes the molten material into the bulk. On the sides, the first mechanism starts to dominate and initiates the ablation of superheated liquid layers, which decompose into vapor immediately as the surrounding pressure drops. In literature, the fast phase transition near the thermodynamic critical point is referred to phase explosion [1]. Noticeably, the liquid material that is ejected radially due to a recoil pressure, is reminiscent to the ablation mechanism observed in nanosecond pulses, as described by [4].

Next, the ablation process depicted in Fig. 6 (same scales as in Fig.5) for the $7.4\mu\text{J}$ and $10.4\mu\text{J}$ pulse energy reveals very similar process dynamics. The only difference is that with increasing pulse energy, we have more energy in the system which yields a broader and deeper melt pool. Further, the layer wise ablation is weaker, and the depression caused radial ejections become more pronounced. This trend is affirmed by the solidified spatters observed in Fig.3, which are dispersed radially at greater distances compared to those at $3.8\mu\text{J}$. In the case of $7.4\mu\text{J}$, where ablation depth and crater geometry closely align with the experiment, we are confident that the physics involved are accurately captured. However, the considerable discrepancy concerning the ablation depth for the $10.4\mu\text{J}$ simulation indicates a necessity for further model refinement. As previously argued in section 3.1, one potential source for the offset could be numerical inaccuracy in modeling the absorption or the ballistic electron penetration depth. Another factor contributing to the discrepancies could be the modeling or selection of thermodynamic properties under extreme conditions of high temperatures and pressures, particularly within the thermodynamic critical range encountered at these high fluences. In this regard, it is necessary to critically evaluate the choice of elusive temperature-dependent material properties for the liquid copper (cf. Table 1): Firstly, the assumed density 3000kg/m^3 at the critical temperature is simply the linear extrapolation of the densities at melting and boiling point. In fact, our model needs the uncompressed temperature dependent value, *i.e.* the theoretical density at critical temperature under atmospheric pressure. By adjusting the input value to 1900kg/m^3 , which reflects the density at the critical pressure and temperature [7], the ablation depth for the $10\mu\text{J}$ simulation increases approximately by 100nm . Unfortunately, this adjustment also results in elevated ablation depths at lower pulse simulations. Secondly, the bulk modulus (cf. [9]) is only documented up to 2400K . The subsequent temperature-dependent decay is estimated based on the premise that the liquid and vapor bulk moduli converge at the critical point. But the significant reduction of approximately four

orders of magnitude raises questions regarding the manner in which the function declines. To illustrate the impact of the bulk modulus and density prescribed for the superheated liquid copper, Fig. 7 presents results of two variations of the simulation with $7.4\mu\text{J}$. In Fig. 7a) the bulk modulus is maintained at a constant value of $5 \cdot 10^9 \text{ Pa}$, and in Fig. 7b), the density is kept constant at 6792kg/m^3 after exceeding the boiling temperature. When the bulk modulus does not decrease towards the critical temperature, a greater proportion of energy is allocated to expanding the liquid rather than compressing it. As a result, the upwards impulse becomes dominant yielding immediate ablation of the material, and no radial ejection can take place. *Vice versa*, when the density does not decrease towards the critical temperature, the opposite happens, and melt is ejected primarily radially. This interplay is evidenced by the absence of ring structures in the crater of Fig. 7a) and the presence of ring structures in Fig. 7b). Furthermore, the ablation depths are significantly lower than in the original simulation and experiment, namely about 250 and 700nm , respectively.

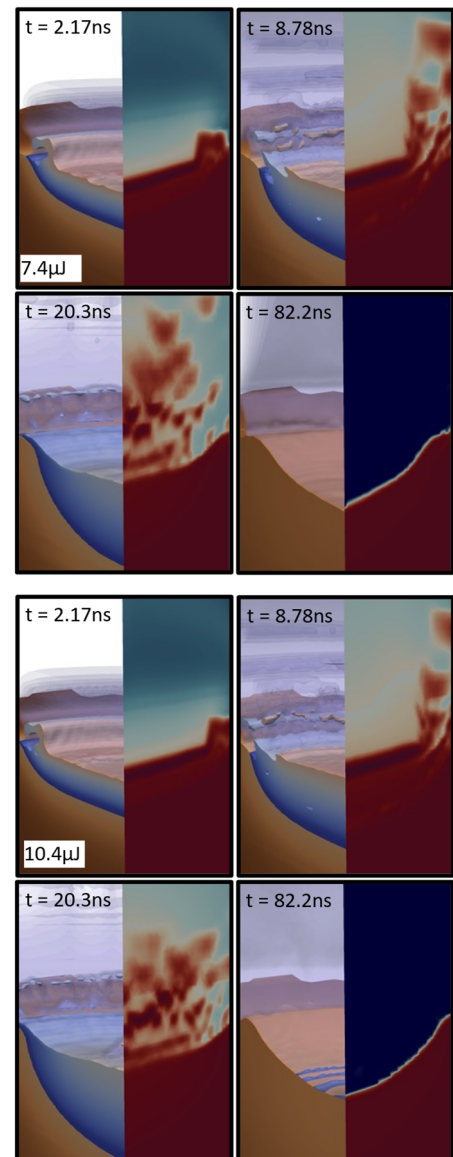


Fig.6. Ablation mechanism at $7.4\mu\text{J}$ pulse energy (890nm max ablation depth) and $10.4\mu\text{J}$ pulse energy (930nm max ablation depth)

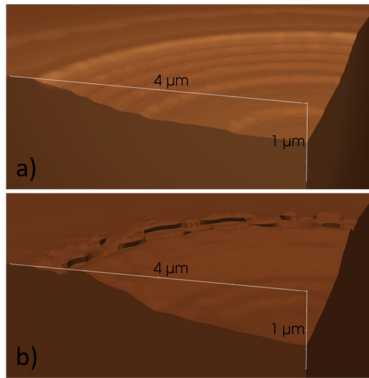


Fig.7. Variation in material parameters for 7.4 μ J pulse energy simulation a) constant bulk modulus and b) constant density for superheated liquid copper

Thus, the selected estimated values appear to be an acceptable compromise for pulse energies up to 7.4 μ J. For more extreme conditions, such as encountered at 10.4 μ J, either the simulation model requires an extension to include special considerations towards the critical point or more sophisticated theoretical models to better refine the material properties.

Finally, Fig. 8 illustrates the ablation mechanism at the lowest pulse energy in investigation. In the initial frame, a melt pool depression induced by vaporization, as well as an ongoing melting process can be seen. Then, at $t=0.47$ ns, the final amount of material is melted resulting in a greater volume expansion and an increased momentum upwards. At this stage, we already see the onset of a liquid layer evolving, which is subsequently detached at $t=2.17$ ns in a concave shape. Compared to higher pulse energies, we do not encounter any ring shape at the edge of the crater, which aligns with the experimental findings. The mechanism, the shape of the ablated layer and the crater resembles the observations reported in [10].

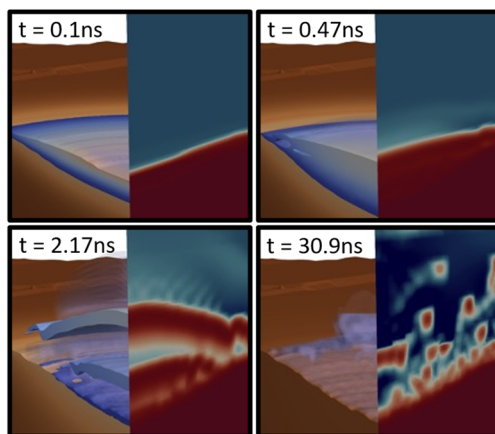


Fig.8. Ablation mechanisms at 1 μ J pulse energy (max. ablation depth 280nm)

4. Summary and Outlook

This work is an extension to our previously published multiphysics simulation tool [2] for laser material processing, in order to represent the intricate physics accompanied in laser micro processing with high power femtosecond lasers. The implementation of the two-temperature model as well as a Drude absorption model is tested upon a broad range of

fluences ranging from 6 to over 60J/cm². The simulations accurately align the experimental observations for intermediate fluences up to 45J/cm² (7.4 μ J for the underlying pulse energy and beam diameter) regarding ablation depth and crater geometry. In this range, the model has shown its potential in capturing the complex interplay between energy deposition and material response. Thereby, the thorough 3-dimensional model makes predictions concerning ablation depth, ablation mechanism and crater topology feasible. The findings of this study agree well with the literature and complements the state of the art by a mesoscopic process understanding.

Future investigation will aim to address the uncertainties associated with modeling and describing elusive material parameters and their interplay within the thermodynamic critical range. Furthermore, the model will be used to shed further light on the effects of parameter variations such as pulse length, fluence and the influence of target materials. Also, the model will be used to predict crater and drill hole features for multipulse processes.

Acknowledgements

T. Florian gratefully acknowledges funding through the FWF within the project “Formidable” (6401-N).

References

- [1] X. Li, Y. Guan, Theoretical fundamentals of short pulse laser–metal interaction: A review, *Nanotechnology and Precision Engineering*. 3 (2020) 105–125.
- [2] C. Zenz, M. Buttazzoni, T. Florian, K.E. Crespo Armijos, R. Gómez Vázquez, G. Liedl, A. Otto, A compressible multiphase Mass-of-Fluid model for the simulation of laser-based manufacturing processes, *Computers & Fluids*. 268 (2024) 106109.
- [3] C.W. Cheng, S.Y. Wang, K.P. Chang, J.K. Chen, Femtosecond laser ablation of copper at high laser fluence: Modeling and experimental comparison, *Applied Surface Science*. 361 (2016) 41–48.
- [4] K.H. Leitz, B. Redlingshöfer, Y.Reg, A. Otto, M. Schmidt, Metal Ablation with Short and Ultrashort Laser Pulses, *Physics Procedia* 12 (2011) 230–238.
- [5] S. Tratra, R. Gomez Vasquez, C. Stiglbrunner, A. Otto, Numerical simulation of laser ablation with short and ultra-short pulses for metals and semiconductors, *Physics Procedia* 83 (2016) 1339 – 1346.
- [6] S.E. Kirkwood, Y.Y. Tsui, R. Fedosejevs, A.V. Brantov, V.Yu. Bychenkov, Experimental and theoretical study of absorption of femtosecond laser pulses in interaction with solid copper targets, *Phys. Rev. B*. 79 (2009) 144120.
- [7] H. Hess, Critical Data and Vapor Pressures for Aluminum and Copper, *International Journal of Materials Research*, 2021, 10.3139.
- [8] J.A. Cahill, A.D. Kirshenbaum, The density of liquid copper from its melting point (1356°K) to 2500°K and an estimate of its critical constants, *The Journal of Physical Chemistry Volume 66, Issue 6, 1961, 10.1021*.
- [9] R.N. Singh, S. Arafin, A.K. George, Temperature-dependent thermo-elastic properties of s-, p- and d-block liquid metals, *Physica B* 387 (2007) 344-351.
- [10] M. Spellauge, J. Winter, S. Rapp, C. McDonnell, F. Sotier, M. Schmidt, H. P. Huber, Influence of stress confinement, particle shielding and re-deposition on the ultrashort pulse laser ablation of metals revealed by ultrafast time-resolved experiments, *Applied Surface Science*, Volume 545, 2021,10.1016.
- [11] J. Byskov-Nielsen, J.-M. Savolainen, M. Christensen, P. Balling, Ultra-short pulse laser ablation of metals: threshold fluence, incubation coefficient and ablation rates, *Appl. Phys. A* 101 (2010) 97–10.
- [12] K. M. Yoo, X. M. Zhao, M. Siddique, R. R. Alfana, D. P. Osterman, M. Radparvar, and J. Cunniff, Femtosecond thermal modulation measurements of electron-phonon relaxation in niobium, *Appl. Phys. Lett.* 56, 1908–1910 (1990).